AGU ADVANCING EARTH AND SPACE SCIENCES

Geophysical Research Letters

RESEARCH LETTER
10.1029/2023GL108068

Three-Dimensional Numerical Modeling of Coseismic Atmospheric Dynamics and Ionospheric Responses in Slant Total Electron Content Observations

P. A. Inchin[1,2], Y. Kaneko[3], A.-A. Gabriel[4,5], T. Ulrich[5], L. Martire[6], A. Komjathy[6], J. Aguilar Guerrero[1], M. D. Zettergren[1], and J. B. Snively[1]

[1]Center for Space and Atmospheric Research, Embry-Riddle Aeronautical University, Daytona Beach, FL, USA, [2]Computational Physics, Inc., Springfield, VA, USA, [3]Department of Geophysics, Kyoto University, Kyoto, Japan, [4]Scripps Institution of Oceanography, University of California San Diego, La Jolla, CA, USA, [5]Department of Earth and Environmental Sciences, Ludwig-Maximilians-University, Munich, Germany, [6]Jet Propulsion Laboratory, California Institute of Technology, Pasadena, CA, USA

Abstract Despite routine detection of coseismic acoustic-gravity waves (AGWs) in Global Navigation Satellite System (GNSS) total electron content (TEC) observations, models of the earthquake-atmosphere-ionosphere dynamics, essential for validating data-driven studies, remain limited. We present the results of three-dimensional numerical simulations encompassing the entire coupling from Earth's interior to the ionosphere during the M_w 7.8 2016 Kaikoura earthquake. Incorporating the impact of data/model uncertainties in estimating the ionospheric state, the results show a good agreement between observed and simulated slant TEC (sTEC) signals, assessed through a set of metrics. The signals exhibit intricate waveforms, resulting from the integrated nature of TEC and phase cancellation effects, emphasizing the significance of direct signal comparisons along realistic line-of-sight paths. By comparing simulation results initialized with kinematic and dynamic source models, the study demonstrates the quantifiable sensitivity of sTEC to AGW source specifications, pointing to their utility in the analysis of coupled dynamics.

Plain Language Summary Earthquakes launch acoustic-gravity waves (AGWs) into the atmosphere, spanning periods from seconds to minutes, that can reach the ionosphere at ~100–400 km altitude. The majority of AGW detections in the ionosphere are performed with the use of GNSS signals collected with ground-based receivers that nowadays comprehensively cover seismically active regions. However, the modeling of earthquake-atmosphere-ionosphere processes together, essential for validating and supporting data-driven studies, remains rare. We present the outcomes of three-dimensional numerical modeling of interconnected processes, spanning from Earth's interior to the ionosphere. We conducted a case study focused on the 2016 M_w 7.8 earthquake in New Zealand, renowned for its complexity and comprehensive observations of coseismic AGWs recorded with GNSS signals. Our results demonstrate a high level of accuracy of simulated GNSS signals, also revealing the high sensitivity to the chosen earthquake model and the complexity of resulting ionospheric signals, highlighting the necessity of attributing realistic geometries of GNSS TEC observations. The findings highlight the potential for using GNSS signals to investigate coseismic AGWs to infer characteristics of earthquakes.

Key Points:

- Acoustic-gravity wave-driven slant total electron content (sTEC) signals are analyzed in terms of amplitude, waveform, and onset time
- Intricate sTEC signal waveforms result from ionospheric fluctuations measured along lines-of-sight between satellites and receivers
- High sensitivity of sTEC signals to acoustic-gravity wave source specification provides additional basis for earthquake characterization

Supporting Information:

Supporting Information may be found in the online version of this article.

Correspondence to:

P. A. Inchin,
pinchin@cpi.com

Citation:

Inchin, P. A., Kaneko, Y., Gabriel, A.-A., Ulrich, T., Martire, L., Komjathy, A., et al. (2024). Three-dimensional numerical modeling of coseismic atmospheric dynamics and ionospheric responses in slant total electron content observations. *Geophysical Research Letters*, *51*, e2023GL108068. https://doi.org/10.1029/2023GL108068

Received 5 JAN 2024
Accepted 9 OCT 2024

1. Introduction

Seismically excited acoustic and acoustic-gravity waves (here, AGWs) in the atmosphere serve as sources of detectable ionospheric plasma density fluctuations (Blanc, 1985; Ducic et al., 2003; Hines, 1960; Tanaka et al., 1984). By AGWs, we include the spectrum of compressional atmospheric waves and modes ranging from infrasonic acoustic waves, primarily ≤1 Hz, down to the acoustic cut-off frequency in the middle thermosphere corresponding to a period ≥10 min. The terminology "AGW spectrum" thus acknowledges that acoustic waves that have evolved to longer periods in the thermosphere (i.e., by nonlinear evolution) may exceed the Brunt-Väisälä period in the upper mesosphere and lower thermosphere, requiring the consideration of gravity and the use of an acoustic-gravity wave dispersion relation in analysis or modeling of their long-range propagation.

Above earthquakes and other natural hazards, the low-frequency acoustic regime of the AGW spectrum is routinely detected by measuring delays of Global Navigation Satellite System (GNSS) signals to infer

fluctuations in total electron content (TEC), which is directly proportional to the integrated number of electrons along the path between a GNSS satellite and a ground-based receiver (e.g., Hofmann-Wellenhof et al., 2007). The distribution of GNSS receivers in seismically active regions, the tracking of signals from multiple GNSS constellations, as well as the advancements in temporal resolution of measurements, have significantly bolstered the use of TEC for the detection and analysis of coseismic AGWs (Astafyeva, 2019; Calais & Minster, 1995; Komjathy et al., 2016; Occhipinti et al., 2013). The studies rely on the temporal and spatial characteristic variability of TEC signals, including arrival times (Astafyeva & Shults, 2019; Sanchez et al., 2023; Thomas et al., 2018), amplitudes (Cahyadi & Heki, 2014; Inchin et al., 2021; Manta et al., 2020), and shapes (Astafyeva & Heki, 2009; Bagiya et al., 2023; Brissaud & Astafyeva, 2022), showing promise for enhancing the operational capabilities of systems that monitor AGW fluctuations in the ionosphere (Maletckii & Astafyeva, 2021; Manta et al., 2021; Martire et al., 2023; Ravanelli et al., 2021; Savastano et al., 2017).

At the same time, simulations of earthquake-atmosphere-ionosphere processes, essential for validating data-driven studies, remain challenging. First, the development of comprehensive earthquake source models is essential and necessitates a thorough consideration of the rupture process to address resulting atmospheric dynamics (Astafyeva & Heki, 2009; Bagiya et al., 2018; Nozuka et al., 2024). Second, high-resolution three-dimensional nonlinear and compressible atmospheric models are required for simulating AGWs with periods ranging from seconds to minutes (Inchin, Snively, Williamson, et al., 2020). The resolution of AGWs is required over comparatively large regions to cover line-of-sights (LOS) between GNSS satellites and ground-based receivers. Third, the direct modeling of ionospheric responses to AGWs is also crucial, taking into account potential nonlinear behavior and the complexity of plasma responses to neutral gas drivers within ambient geomagnetic field (Zettergren & Snively, 2015, 2019). Atmospheric and ionospheric simulations must effectively account for background states and winds, which influence AGW propagation and resulting plasma drifts (Drob et al., 2003; McDonald et al., 2012). The scope and complexity of these processes necessitate a comprehensive analysis of the dynamics at every step and in every system.

The magnitude 7.8 Kaikoura earthquake struck the South Island of New Zealand on 13 November 2016 T_0 = 11:02:56 UT (11/14/2016, 00:02:56 local time) and resulted in more than 20 fault segments ruptured, including some previously unknown or considered inactive. Despite the availability of various geophysical data sets, the complete understanding of its rupture evolution remains elusive, positioning this earthquake as one of the most intricate records to date (Hamling et al., 2017; Kaiser et al., 2017). Despite this, the ionospheric responses to coseismic AGWs were measured by a substantial number of multi-GNSS receivers across New Zealand. These detections offered an opportunity to investigate and quantify coseismic processes for an inland earthquake together with ionosphere responses and to propose new techniques for earthquake source characterization (Bagiya et al., 2018; Inchin et al., 2021; Lee et al., 2018; Zedek et al., 2021).

We report new results leveraging our fully 3D modeling approach for simulating earthquake-atmosphere-ionosphere coupling processes, applied to the M_w 7.8 Kaikoura earthquake and its associated TEC signals. We investigate the structure of electron density fluctuations along LOSs and the resulting sTEC signals, and assess the impacts of uncertainties in estimating background ionospheric states (based on absolute TEC) on these fluctuations. In addition to simulations utilizing the earthquake's kinematic source model, we here compare to simulations with a multi-fault dynamic rupture earthquake source model.

2. Methodology

We conducted 3D seismic wave propagation simulations with the specification of kinematic and dynamic earthquake source models. The first two simulations (referred to as Sim 1 and Sim 2) corresponds to the kinematic source model of Inchin et al. (2021), constrained by strong-motion, InSAR, Global Positioning System (GPS), vertical coastal uplift and tsunami data, and was used to initialize a SPECFEM3D simulation (Komatitsch & Tromp, 2002; Komatitsch & Vilotte, 1998). To address the uncertainty in estimation of absolute vTEC, expected to be at the level ∼1–6 TECu (e.g., Chen et al., 2020; Ren et al., 2019; Roma-Dollase et al., 2018; Wielgosz et al., 2021), and its role in determining AGW signals in sTEC (∼0.02–0.2 TECu), we conducted two 3D GEMINI simulations corresponding to the background ionospheric conditions at the time of the earthquake T_0 and T_0-30 min (Sim 1 and Sim 2, respectively), but with the same seismic wave propagation and AGW simulation inputs with kinematic source model. Third simulation, Sim 3, included coupled dynamic source model and wave propagation simulation, which was conducted with the SeisSol software (Breuer et al., 2014; Dumbser &

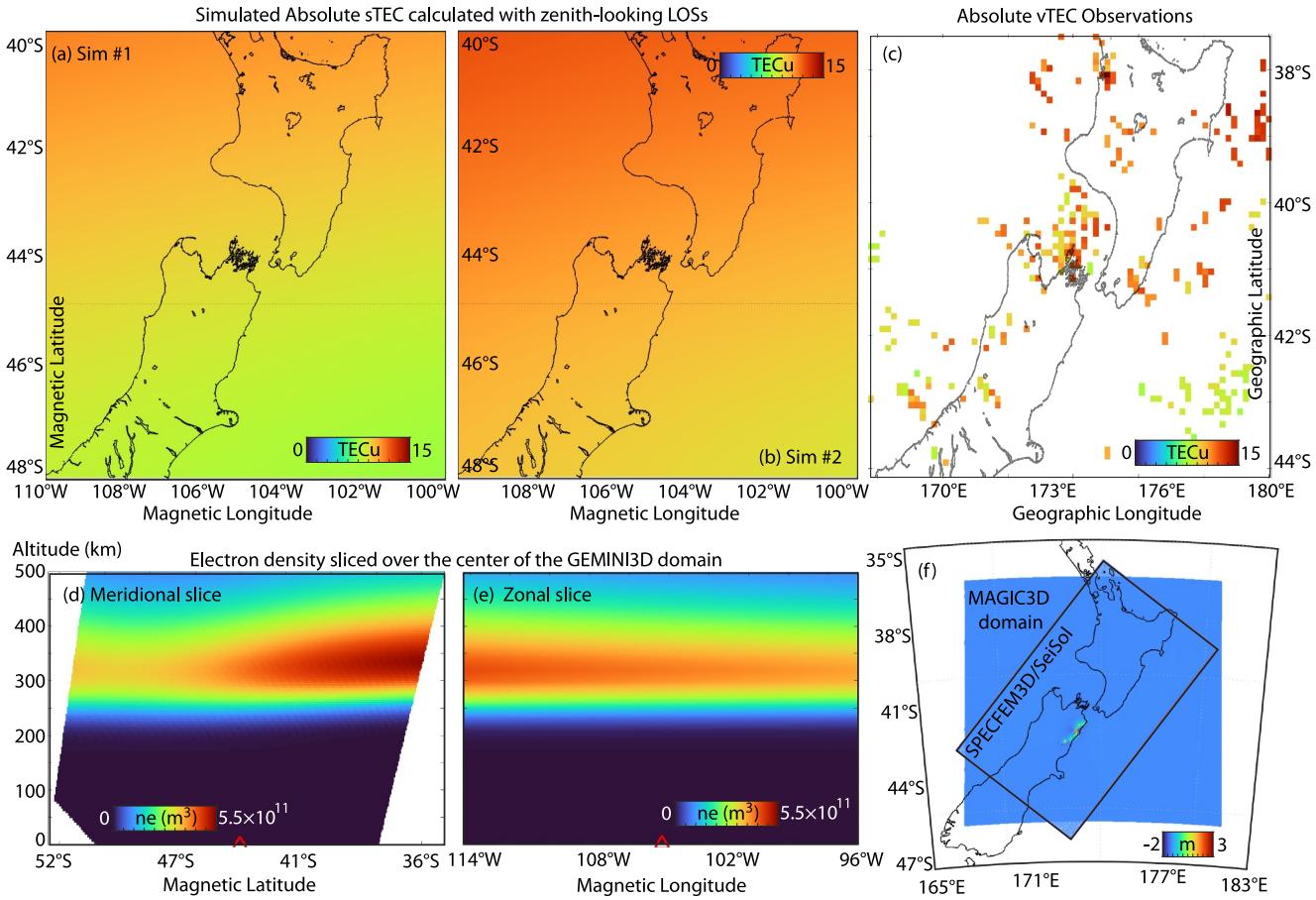

Figure 1. Absolute simulated sTEC calculated with zenith-looking LOSs at (a) 11:02:56 UT (Sim 1) and (b) 10:32:56 UT (Sim 2). (c) Observations of absolute vTEC at 11:00 UT. (d, e) Meridional and zonal slices of simulated electron density at 11:02:56 UT. (f) Schematic representation of the overlay of numerical domains used for SPECFEM3D/SeisSol and MAGIC simulations. The colors show maximum vertical velocities at the surface from the SPECFEM3D simulation for illustrative purposes.

Käser, 2006; Pelties et al., 2013; Uphoff et al., 2017) with dynamic source model described in Ulrich et al. (2019). Sim 3 was run at the original time of the earthquake T_0, as Sim 1. The summary of simulation setups is provided in Table S1 of the Supporting Information S1.

Coupling with 3D nonlinear and compressible neutral atmosphere model MAGIC was made through the transfer of vertical momentum at the surface (Inchin, Snively, Zettergren, et al., 2020). The overlay of numerical domains used for SPECFEM3D/SeisSol and MAGIC simulations is illustrated in Figure 1f. MAGIC simulations were configured with a spatial resolution of 500 m in horizontal and 250 m in vertical directions. Atmospheric stratification and winds were based on global empirical models NRLMSISE-00 and HWM-14 (Drob et al., 2015; Picone et al., 2002), and covered the heights from the surface to 500 km, with ~9 × 17.7° in meridional and zonal directions. Geomagnetic indexes Kp and Dst during the events were 3 and -20 nT, respectively. The 3D output of the MAGIC simulations, including perturbations in major gas species densities, temperature, and fluid velocities, served as drivers in the three-dimensional ionospheric model GEMINI. The basis for MAGIC and GEMINI are described in Zettergren and Snively (2015).

Slant TEC (sTEC) observations, representing the total number of electrons along a path between receiver and satellite and derived based on the measurements of phase advances and group delays at two GNSS signals (e.g., Komjathy, 1997), were calculated using software developed at the Jet Propulsion Laboratory gnsstec. py (JPL New Technology Report 52,034, Bertiger et al. (2020)) and GIM (Mannucci et al., 1998). We utilized raw GPS and GLONASS navigation and observation data at a sampling rate of 1 Hz in Receiver Independent Exchange Format (RINEX). For observations, the height of 300 km was specified as ionospheric shell layer to calculate ionospheric pierce point (IPP) positions. Vertical TEC (vTEC), which represents scaled sTEC from the geocenter

and through IPP positions (e.g., Mannucci et al., 1998), was estimated using a Single Layer Mapping function. Model synthesized sTEC signals were calculated from the integration of electron densities (n_e), based on the outputs of n_e from GEMINI simulations. To compare measured and simulated sTEC signals along temporally and spatially varying LOS, we applied a Butterworth filter with a fourth-order and a window of 30–600 s.

3. Results

3.1. Ionospheric Responses to Coseismic AGWs

The results of seismic wave propagation simulations with a kinematic source model and atmospheric dynamics were presented by Inchin et al. (2021), whereas here we focus on fully 3D ionospheric plasma responses to AGWs and sTEC signals. During the local night-time of the event, the absolute vTEC exhibited values ranging between 6 and 14 TEC units (TECu) across New Zealand (Figure 1c). While a broad positive gradient of vTEC is evident from south to north, the observations reveal intricate variations in vTEC, potentially attributable to ionospheric disturbances of diverse origins. Figures 1a and 1b depicts the absolute vTEC from Sim 1 and Sim 2 simulations. Simulated vTEC ranges from ∼5–7 TECu at the south to ∼11–14 TECu over the Northern Island, giving difference between the simulations of 2–5 TECu over the numerical domain. Figures 1d and 1e illustrate n_e fields from Sim 1 along the meridional and zonal directions with altitudes, respectively, sliced over the center of GEMINI domain. The electron density peak altitude (hmF2) from simulations is at ∼300 km, reaching values of 5.5×10^{11} m^{-3}.

Figures 2a–2d illustrate the snapshots of simulated sTEC fluctuations, assuming zenith-looking LOSs. The leading fluctuations, surpassing the typical noise level of TEC at ∼0.01–0.02 TECu, become discernible ∼10 min after T_0. The time required for the rupture propagation spans over ∼90 s, with the most pronounced AGWs being generated ∼60–80 s after the rupture initiation (Inchin et al., 2021). The leading fluctuations are slightly inclined toward the northeast, aligning with the direction of rupture propagation. They arise from n_e perturbations occurring at altitudes of ∼230–250 km, revealing plasma drifts not fully aligned with magnetic field lines and influenced by larger neutral-ion collision frequency at these altitudes. The largest amplitude sTEC fluctuations, calculated with zenith-looking LOS geometries, are simulated over the region between the North and South Islands of New Zealand (∼39-41°S/172-175°E), with the positive phase reaching this area ∼12 min after T_0. As plasma drifts from AGWs are primarily aligned with magnetic field lines (Inchin et al., 2021; Zettergren & Snively, 2015), the simulated electron density fluctuations, as can be seen from sTEC, dominantly evolve equatorward (Figures 2c and 2d).

Figure 2e displays the field of peak absolute amplitudes of sTEC fluctuations (zenith-looking LOS geometry as in panels a–d). Figure 2f shows neutral major gas temperature perturbations (their moduli) at 300 km altitude. The largest amplitude temperature perturbations from AGWs are found to the north and northeast of the epicenter, arising from the northeastward propagation of the rupture and focusing of AGWs. At the same time, the largest amplitude sTEC fluctuations, up to 0.26 TECu, are observed over the region between the North and South Islands of New Zealand (Figure 2e). The fluctuations to the west and south from the epicenter, as well as offshore to the east, also exhibit amplitudes higher than TEC noise level, in the range of ∼0.02–0.08 TECu. The disparities between the illustrated fields of peak amplitudes of sTEC fluctuations (panel e) and AGW-driven perturbations in the neutral atmosphere at 300 km altitude (panel f) highlight the importance of the alignment of plasma drifts driven by AGWs along magnetic field lines, exhibiting dominant equatorward motion, even in the present of large amplitude dynamics in the neutral gas (Bagiya et al., 2017; Rolland et al., 2013; Zettergren & Snively, 2015).

Simulated n_e fluctuations for six satellite-station pairs along their actual LOSs with time are presented in the top panels of Figures 2g–2l. Their Y axes are altitudes along respective LOSs. To obtain n_e fluctuations along LOSs, we additionally performed GEMINI simulation excluding AGWs drivers, and then subtracted its 3D fields of n_e from the 3D fields of n_e calculated in the simulation which included AGWs (Sim 1). In the corresponding bottom panels, we show the resultant sTEC fluctuation signals (black lines). To avoid filtering artifacts, here sTEC fluctuations are calculated by directly subtracting absolute sTEC from simulations with and without AGWs. The altitude of the largest amplitude n_e fluctuations along the respective LOS are illustrated with red lines.

The onset time of sTEC signals corresponds to altitudes ∼230–260 km, depending on the elevation angle and positioning of LOS. This suggests that sTEC signals are sensitive to AGW-driven fluctuations at altitudes significantly lower than hmF2. The complexity of n_e fluctuations along the LOS demonstrates the fact that they, and thus sTEC signals, do not originate from a single, fixed altitude. Instead, this altitude varies in accordance

10.1029/2023GL108068

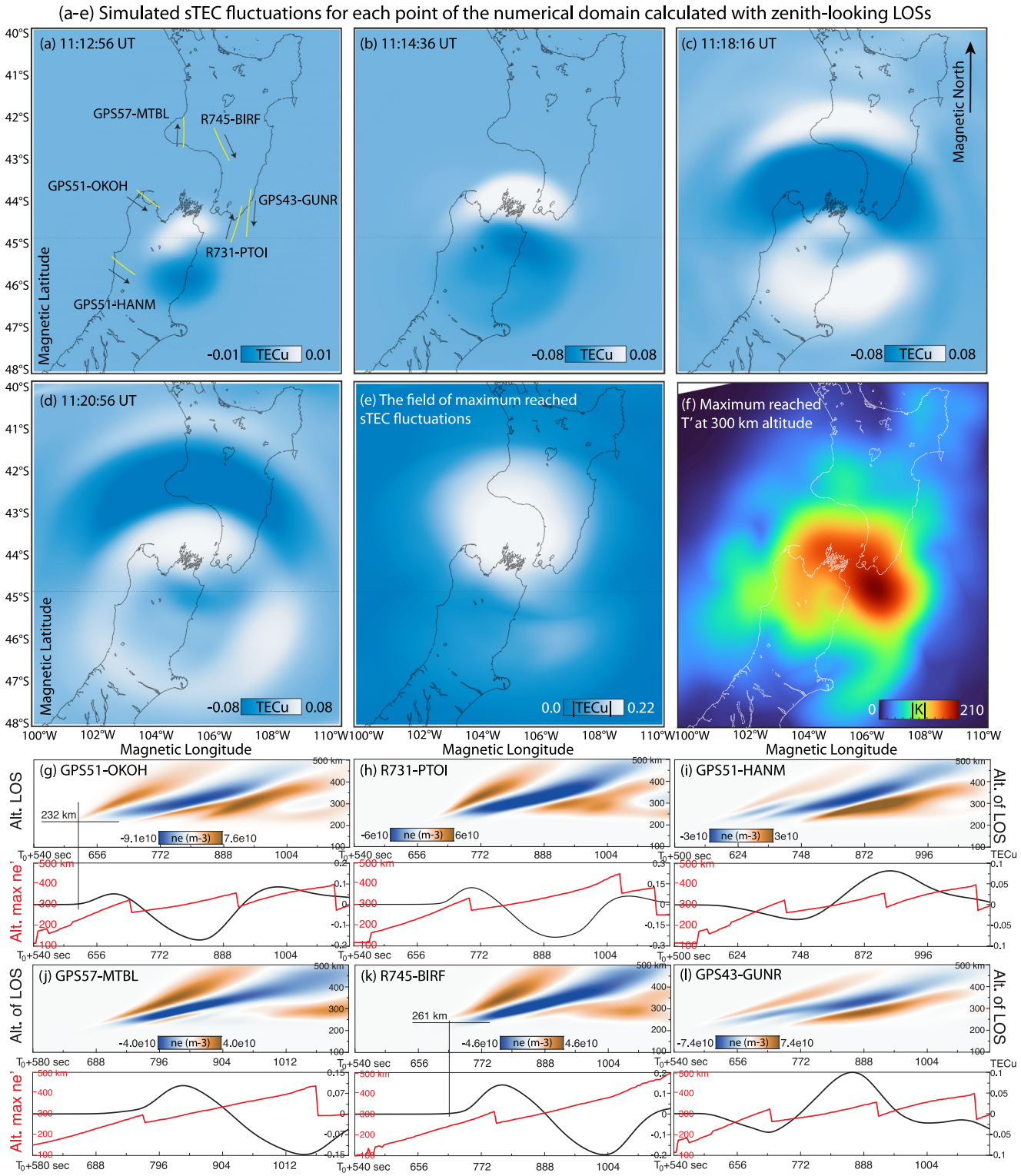

Figure 2. (a–d) The snapshots of simulated sTEC fluctuations calculated for each point of the numerical domain with zenith-looking LOSs at four epochs and (e) the field of their maximum values (moduli) calculated over the whole time of simulation. (f) Maximum neutral major gas temperature perturbations (moduli) at 300 km altitude calculated over the whole time of simulatio. (g–l) Electron density (n_e) fluctuations over the time along realistically spatially and temporally varying LOSs and resulting sTEC signals (black lines) and the altitudes of maximum n_e fluctuations (red lines). The IPP positions for satellite-station pairs in panels g–l are shown in panel a with yellow lines for 20 min from T_0.

with the evolving plasma drifts over time. While the initial fluctuations in sTEC may arise from n_e fluctuations contributing at lower altitudes, the peak amplitudes of these signals can result from heights close to hmF2 or higher at 400–500 km.

The nature of sTEC, which involves integrating n_e along the LOS, can introduce complexities that lead to the potential cancellation of otherwise detectable fluctuations. This is demonstrated in panels i and l of Figure 2, where the initial positive n_e fluctuations along the LOS (top panels), although present, contribute minimally to the resulting sTEC signals (respective bottom panels). Subsequent negative n_e fluctuations then dominate in contribution to sTEC, ultimately resulting in an apparent initial negative phase in sTEC fluctuation signals. The phase-cancellation effect (i.e., when the LOS pierces positive and negative phases of n_e fluctuations, eventually returning a smaller amplitude sTEC fluctuation signal than if piercing only positive or negative phases of n_e fluctuations, e.g., Manta et al. (2020)) may lead to signals falling below TEC noise level, as demonstrated for the GPS51-HANM pair. Such dynamics of n_e fluctuations, as shown in panels i and l, also imply an apparent delayed detectability of sTEC (onset time) when observed with an unsuitable LOS. Likewise, the period and shape of these signals vary depending on the alignment of plasma drifts relative to the LOS.

3.2. Comparison of Observed and Synthetic sTEC Signals

Figure 3 provides a comparison between observed and simulated sTEC signals. The focus of our analysis lies within observations taken over the main group, as shown on the map in Figure 3. The other groups of observations originated from areas west of the epicenter, spanning over North Island of New Zealand, and over the ocean to the east of the epicenter. Although still finding a sufficient level of agreement with observations, we omitted most signals originating to the south of South Island, as they consistently exhibited signal amplitudes below expected TEC noise level. Simulated sTEC signals in Figure 3 are calculated along actual LOSs, that is, in the same geometry as they were observed during the event.

First, we find that the variability of the background ionospheric state between Sim 1 and Sim 2 does not translate into a notable difference in simulated sTEC signals and neither of the simulations outperformed when compared with the observations. Thus, for the event considered here, we expect that the presented uncertainty associated with absolute vTEC may not necessarily be a source of error when simulating sTEC signals driven by AGWs. However, we expect that larger discrepancies in absolute vTEC or variations in the ionospheric layering unrelated to the event may lead to more significant differences in simulated sTEC fluctuations.

The highest level of agreement of simulated and observed sTEC signals is over the region between North and South Islands of New Zealand with a similar level of concordance to the west and northwest of the epicenter. A common trend of smaller amplitudes in the simulated signals over Northern Island is noted. Here, despite closely matching the shapes of the signals and onset times, simulated sTEC consistently exhibit ∼50% lower amplitudes. Separately, analyzing sTEC signals to the east of the epicenter, we find that their amplitudes are effectively captured by simulations, but they appear ∼20 s earlier in time than the observed ones. Lastly, Figure 3 presents a comparison of signals located to the south of the epicenter, which mostly agree, but exhibit limited utility due to low signal-to-noise ratio. Understanding the causes of sTEC discrepancies for some satellite-station pairs to the north and east require further in-depth parametric investigation.

To quantify the differences between simulated and observed sTEC, we implemented a set of metrics, including the time of flight (TOF), maximum and minimum amplitudes, the duration of pulses, and the temporal track cross-correlation of signals. An example of metrics estimation is presented for pair GPS51-LEVN in Figure 3 and full metric analysis is provided in the SI (Tables S2–S5 in Supporting Information S1). The TOF error is determined as the difference between the observed and simulated sTEC fluctuation onset times. The onset time is identified as the point at which the derivative of the sTEC signal exceeds the trend four times. Maximum and minimum amplitudes, as well as the duration, for both synthetic and observed sTEC signals, are calculated for the main pulse, which falls between signal onset time and the point where the N-shaped pulse crosses zero amplitude from negative (see pair GPS51-LEVN for reference). The cross-correlation coefficient R, providing the linear dependence between observed and synthetic signals, is calculated for filtered observed and simulated sTEC time series for each satellite-station pair over a period from 120 s before the observed TOF to the last simulated time

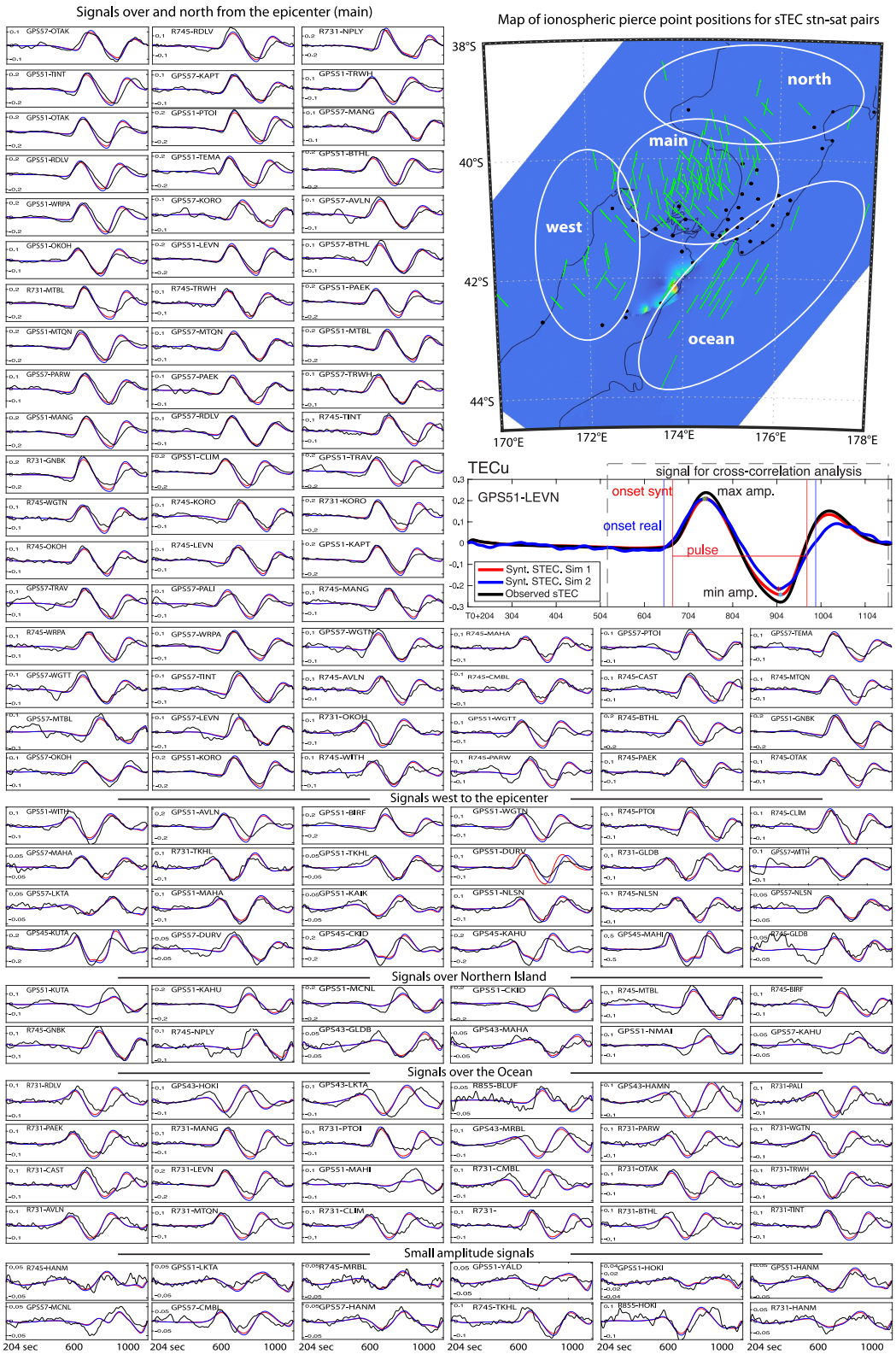

Figure 3. The comparison of observed (black lines) and simulated sTEC signals from Sim 1 (red lines) and Sim 2 (blue lines). Simulated sTEC signals are calculated along temporally and spatially varying LOSs, as measured during the event. Metrics analysis is presented for pair GPS51-LEVN. The time window from T_0 + 204 toT_0 + 1,164 s is chosen for all sTEC time series demonstrated. The map demonstrates IPP positions of observations. The elongated southwest-northeast rectangle illustrates final vertical displacements from Sim 1.

step T_0 + 1,168 s. The error of cross-correlation reported here and in SI is calculated as (1-R)/100%. The selected subset of 92 satellite-station pairs focuses on clearly identifiable signals of AGWs in sTEC, where metrics could be calculated automatically. Unresolved signals to the north of the North Island, east to the Ocean and south (with sTEC signals close or below the TEC noise level) are excluded from the analysis.

On average, the metric errors are as follows: ∼15 s for TOF, 10.4% for the duration of the pulse, and 12.2% for the temporal track cross-correlation of signals and 17.9% for the maximum and 20.2% for the minimum amplitudes of the pulse. We find relatively small error in the TOF constituting ∼15 s. This error is significantly smaller than the time of AGW arrival from the ground of 600 s, on average (i.e., $Onset_{obs} - T_0$ sec, where $Onset_{obs}$ is observed sTEC fluctuation onset time), implying sufficiently accurate timing of the source model and good estimation of atmospheric speeds of sound and ionospheric fluctuation altitudes relative to layers. Similarly, we find favorable agreement for the temporal cross-correlation of signals and the period of pulses. The error in pulse duration, ∼30 s, is relatively small compared to the total period of the signals, which ranges from ∼300–480 s, implying reasonable constraint on the source spectrum as well as timing considerations. We find higher levels of errors in the amplitudes of simulated fluctuations, which are found to be the most challenging to replicate, but note that these errors (∼0.01–0.04 TECu) are close to the noise level of TEC observations themselves.

3.3. Kinematic Versus Dynamic Earthquake Source Model

We performed a set of simulations using the 3D dynamic rupture (e.g., Harris et al., 2018) earthquake source model proposed by Ulrich et al. (2019), referenced as Sim 3 below. The advantage of dynamic source modeling compared to kinematic models is to account for the physics of spontaneous rupture nucleation, propagation and arrest, which, while more complex, can help to address the problems of non-uniqueness of solutions based on purely data-driven source inversion techniques (e.g., Jia et al., 2023; Taufiqurrahman et al., 2023). Thus, the dynamic model, although less-tuned to describe the observations, serves as a tool for understanding the physics underlying rupture progression, which is especially important for complex earthquakes. Additionally, the ruptured faults and the segment sequence in dynamic model by Ulrich et al. (2019) differs from the kinematic source model by Inchin et al. (2021). The background state of the ionosphere in Sim 3 is specified from Sim 1.

Figures 4a and 4b illustrates the comparison of maximum absolute vertical velocities at the Earth surface between Sim 1 and Sim 3. These values are much higher in Sim 3 than those simulated with the kinematic source model (Sim 1). In particular, Figure 4c demonstrates that the maximum temperature perturbations at 300 km altitude in Sim 3 peak at 321 K and are ∼50% larger than in Sim 1. The SI includes the 3D fields of vertical fluid velocities, as well as figures of their peak amplitude at 300 km altitude. Vertical fluid velocities at 300 km altitude from Sim 3 reach maximum and minimum values of 369 m/s and −760 m/s, exceeding these values from Sim 1 by ∼90%, which are 219 m/s and −400 m/s, respectively.

Although Sim 3 results in larger in amplitude AGWs in the atmosphere than Sim 1, the possibility to infer these differences based on sTEC is yet not clear. Thus, Figure 4d shows sTEC signals from Sim 3 compared with sTEC observations and results of Sim 1. We find markedly larger in amplitude sTEC fluctuations in Sim 3, exceeding the amplitudes of observed signals to ∼70–100%. A common earlier onset times of signals of ∼40–50 s is also evident in Sim 3. This points to the importance of a nonlinear evolution of AGWs to acoustic shock N-waves with height, which then lengthen and exhibit speeds of its leading shock fronts faster than local speed of sound. Likewise, the steepness of the signal is more pronounced in Sim 3 than found in observations or in Sim 1, highlighting the nonlinear evolution of AGWs. Such disagreements between observed and simulated signals are found for practically all sTEC signals (additional figures are provided in the SM) in this case. Thus, the dynamic source model would require additional ingredients to fully capture surface vertical motions (e.g., Kaneko & Goto, 2022; Schliwa & Gabriel, 2024), potentially including GNSS TEC signals of coseismic AGWs as novel constraints.

4. Discussion and Conclusion

We presented the results of novel 3D direct numerical simulations, encompassing the chain of dynamics extending from Earth's interior and surface, to the atmosphere and to the ionosphere in response to the 2016 M_w 7.8 Kaikoura earthquake. They have enabled us to conduct a comparison between observed and simulated GNSS

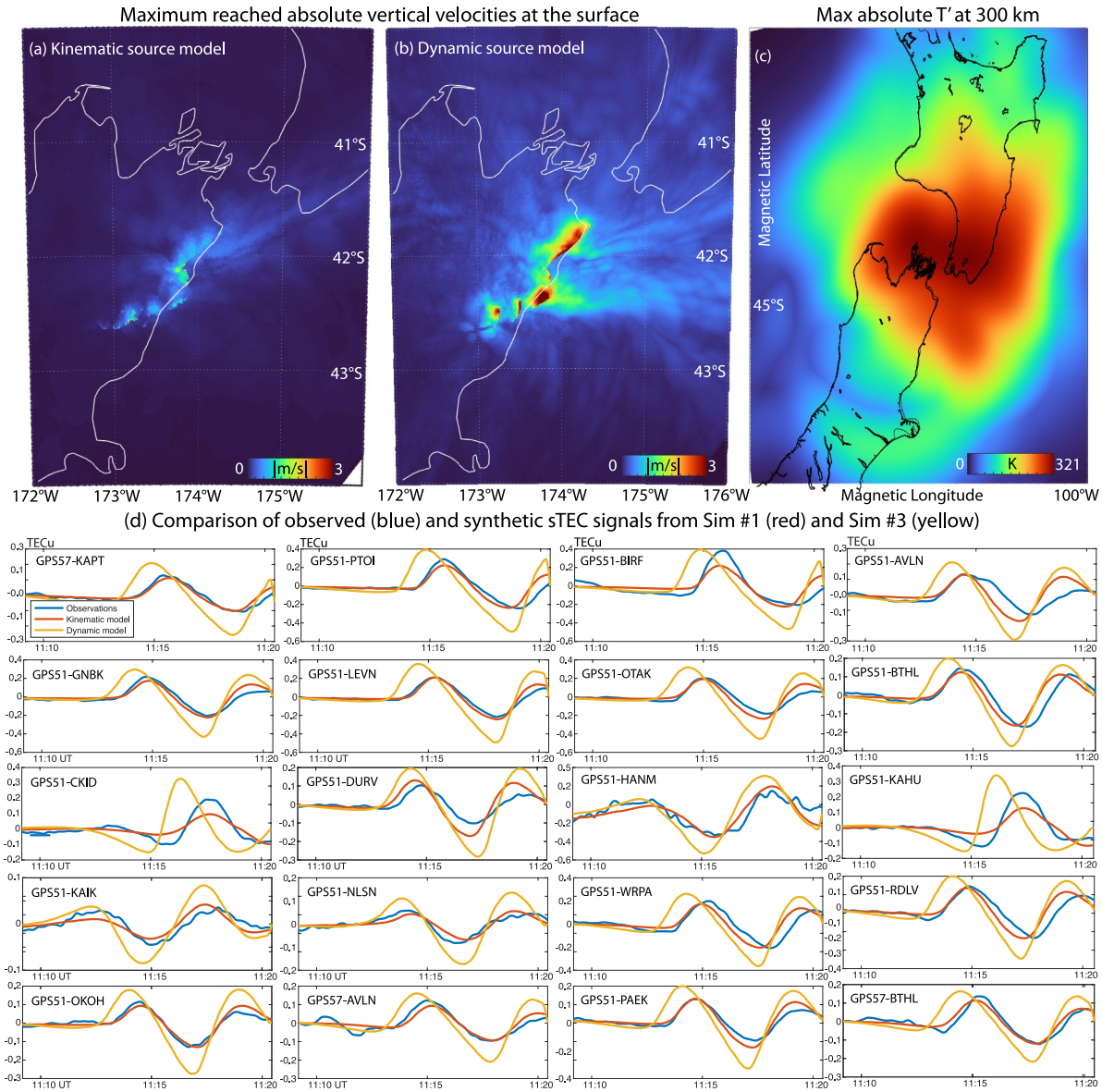

Figure 4. Maximum vertical velocities reached at the Earth's surface calculated based on the (a) kinematic source model (Sim 1) and (b) dynamic source model (Sim 2). (c) Maximum absolute temperature perturbations at 300 km altitude from simulation with dynamic source model. (d) Comparison of sTEC signals as observed (blue lines), derived from Sim 1 (red lines) and Sim 3 (yellow lines).

sTEC signals, considering variations in LOS paths and thus delving into the intricacies of sTEC signals. Our findings highlight that sTEC fluctuation signals, which commonly resemble N-wave shapes (Figure 3), provide a direct representation of AGWs. However, in some cases, the structure of these signals can be significantly influenced by the integration of electron density fluctuations along the LOS. The geometric phase-cancellation effect can result in the attenuation of AGW-driven fluctuations in sTEC signals below TEC noise level, making it challenging to accurately determine signal onset times just relying on data. The results also suggest dominant sTEC signal components originating from different altitudes, above or below the peak of electron density. This questions the common practice of using a fixed IPP height to localize sTEC fluctuations, which are particularly relevant in the context of GNSS TEC observations with low elevation angles, when estimated IPP positions change rapidly. The findings highlight that direct comparisons of simulated and observed sTEC signals along realistic LOS can reduce ambiguity and improve fidelity.

The results demonstrated a high level of agreement between observed and simulated sTEC signals utilizing a kinematic source model, reinforcing the appropriateness of this simulation approach and model specifications for constraining surface motion that drives AGWs. The set of metrics shows promise for applications in the analysis of other seismic events. At the same time, simulations initialized with the dynamic source model find sTEC signal differences reflecting the presence of higher vertical velocities (than simulated with kinematic slip model) at the Earth's surface that act as sources of AGWs. This further highlights the opportunity to employ sTEC signals for constraining surface dynamics during seismic events and to enhance earthquake source models and their validation. Results reinforce the importance of using a large number of observations for the analysis and validation of observational and simulation results, making sTEC particularly attractive to investigate spatially resolved AGW signals in the ionosphere that provide insight into their source geometries and evolutions.

Future studies may clarify the reasons for inconsistencies between synthetic and observed sTEC signals at some station-satellite pairs (Figure 2). For sTEC signals over the northern part of the North Island, it is unlikely that the underestimation of absolute vTEC is the primary cause of such differences, as the difference of several TECu in absolute vTEC between Sim 1 and Sim 2 results in practically unchanged sTEC fluctuation signals. Thus, the discrepancy may be due to under-resolved AGW dynamics in the atmosphere or inaccuracies in the 3D velocity structure assumed in the earthquake model, although no clear correlation is observed between the ground velocity misfit (Figure S2 in Supporting Information S1) and the misfit of sTEC (Figure 3). Similarly, we attribute the temporal lag for a set of signals over the ocean to a potential lack of constraints on rupture propagation offshore, which is less evident based on available geodetic data. These hypotheses can be tested, with development of new kinematic source models, and performance of parametric investigations using the 3D MAGIC-GEMINI capabilities described here.

Conflict of Interest

The authors declare no conflicts of interest relevant to this study.

Data Availability Statement

The SPECFEM3D software is preserved at https://geodynamics.org/resources/specfem3dcartesian, available via the GPL 3 license. The open-source software SeisSol is publicly available: https://github.com/SeisSol/SeisSol with BSD 3-Clause License. GEMINI model is available through https://github.com/gemini3d/gemini3d (Zettergren & Hirsch, 2024) with Apache-2.0 license. GNSS TEC observations used for the investigation of traveling ionospheric disturbances in the study are available at GeoNet Aotearoa New Zealand Continuous GNSS Network AWS Open Data access mechanism https://www.geonet.org.nz/data/access/aws with public access. The Supporting Information S1 to this manuscript are publicly available through ERAU's Data Commons (Inchin P.A. and Snively J.B., 2024).

Acknowledgments
This research is supported by NASA ESI 80NSSC22K0507 and 80NSSC20K0495, DARPA Cooperative Agreement HR00112120003 and HR00112320043, JSPS KAKENHI (21H05206), ERI JURP 2024-S-B103 in Earthquake Research Institute, the University of Tokyo, and the New Zealand eScience Infrastructure (NeSI) HPC Project (gns03247). This work is approved for public release; distribution is unlimited. The content of the information does not necessarily reflect the position or the policy of the Government, and no official endorsement should be inferred. Part of this research was carried out at the Jet Propulsion Laboratory, California Institute of Technology, under a contract with NASA 80NM0018D0004. A.-A.G. and T.U. acknowledge support by the European Union's Horizon 2020 research and innovation programme (Grant number 852992), Horizon Europe (Grant numbers 101093038, 101058129, 101058518), and NSF (Grant numbers EAR-2225286, EAR-2121568, OAC-2139536, OAC-2311208).

References

Astafyeva, E. (2019). Ionospheric detection of natural hazards. *Reviews of Geophysics*, *57*(4), 1265–1288. https://doi.org/10.1029/2019RG000668

Astafyeva, E., & Heki, K. (2009). Dependence of waveform of near-field coseismic ionospheric disturbances on focal mechanisms. *Earth Planets and Space*, *61*(7), 939–943. https://doi.org/10.1186/BF03353206

Astafyeva, E., & Shults, K. (2019). Ionospheric GNSS imagery of seismic source: Possibilities, difficulties, and challenges. *Journal of Geophysical Research: Space Physics*, *124*(1), 534–543. https://doi.org/10.1029/2018JA026107

Bagiya, M. S., Heki, K., & Gahalaut, V. K. (2023). Anisotropy of the near-field coseismic ionospheric perturbation amplitudes reflecting the source process: The 2023 February Turkey earthquakes. *Geophysical Research Letters*, *50*(14), e2023GL103931. https://doi.org/10.1029/2023GL103931

Bagiya, M. S., Sunil, A. S., Sunil, P. S., Sreejith, K. M., Rolland, L., & Ramesh, D. S. (2017). Efficiency of coseismic ionospheric perturbations in identifying crustal deformation pattern: Case study based on mw 7.3 may Nepal 2015 earthquake. *Journal of Geophysical Research: Space Physics*, *122*(6), 6849–6857. https://doi.org/10.1002/2017JA024050

Bagiya, M. S., Sunil, P. S., Sunil, A. S., & Ramesh, D. S. (2018). Coseismic contortion and coupled nocturnal ionospheric perturbations during 2016 Kaikoura, Mw 7.8 New Zealand earthquake. *Journal of Geophysical Research: Space Physics*, *123*(2), 1477–1487. https://doi.org/10.1002/2017JA024584

Bertiger, W., Bar-Sever, Y., Dorsey, A., Haines, B., Harvey, N., Hemberger, D., et al. (2020). Gipsyx/rtgx, a new tool set for space geodetic operations and research. *Advances in Space Research*, *66*(3), 469–489. https://doi.org/10.1016/j.asr.2020.04.015

Blanc, E. (1985). Observations in the upper atmosphere of infrasonic waves from natural or artificial sources: A summary. *Annales Geophysicae*, *3*, 673–687.

Breuer, A., Heinecke, A., Rettenberger, S., Bader, M., Gabriel, A.-A., & Pelties, C. (2014). Sustained petascale performance of seismic simulations with seissol on supermuc. In *Supercomputing: 29th International Conference, ISC 2014, Leipzig, Germany, June 22-26, 2014. Proceedings 29* (pp. 1–18). Springer International Publishing.

Brissaud, Q., & Astafyeva, E. (2022). Near-real-time detection of co-seismic ionospheric disturbances using machine learning. *Geophysical Journal International*, *230*(3), 2117–2130. https://doi.org/10.1093/gji/ggac167

Cahyadi, M. N., & Heki, K. (2014). Coseismic ionospheric disturbance of the large strike-slip earthquakes in North Sumatra in 2012: Mw dependence of the disturbance amplitudes. *Geophysical Journal International*, *200*(1), 116–129. https://doi.org/10.1093/gji/ggu343

Calais, E., & Minster, J. B. (1995). Gps detection of ionospheric perturbations following the January 17, 1994, Northridge earthquake. *Geophysical Research Letters*, *22*(9), 1045–1048. https://doi.org/10.1029/95GL00168

Chen, P., Liu, H., Ma, Y., & Zheng, N. (2020). Accuracy and consistency of different global ionospheric maps released by IGS ionosphere associate analysis centers. *Advances in Space Research*, *65*(1), 163–174. https://doi.org/10.1016/j.asr.2019.09.042

Drob, D. P., Emmert, J. T., Meriwether, J. W., Makela, J. J., Doornbos, E., Conde, M., et al. (2015). An update to the horizontal wind model (HWM): The quiet time thermosphere. *Earth and Space Science*, *2*(7), 301–319. https://doi.org/10.1002/2014EA000089

Drob, D. P., Picone, J. M., & Garcés, M. (2003). Global morphology of infrasound propagation. *Journal of Geophysical Research*, *108*(D21). https://doi.org/10.1029/2002JD003307

Ducic, V., Artru, J., & Lognonné, P. (2003). Ionospheric remote sensing of the Denali Earthquake Rayleigh surface waves. *Geophysical Research Letters*, *30*(18). https://doi.org/10.1029/2003GL017812

Dumbser, M., & Käser, M. (2006). An arbitrary high-order discontinuous Galerkin method for elastic waves on unstructured meshes — II. The three-dimensional isotropic case. *Geophysical Journal International*, *167*(1), 319–336. https://doi.org/10.1111/j.1365-246X.2006.03120.x

Hamling, I. J., Hreinsdóttir, S., Clark, K., Elliott, J., Liang, C., Fielding, E., et al. (2017). Complex multifault rupture during the 2016 Mw 7.8 Kaikoura earthquake, New Zealand. *Science*, *356*(6334). https://doi.org/10.1126/science.aam7194

Harris, R. A., Barall, M., Aagaard, B., Ma, S., Roten, D., Olsen, K., et al. (2018). A suite of exercises for verifying dynamic earthquake rupture codes. *Seismological Research Letters*, *89*(3), 1146–1162. https://doi.org/10.1785/0220170222

Hines, C. O. (1960). Internal atmospheric gravity waves at ionospheric heights. *Canadian Journal of Physics*, *38*(11), 1441–1481. https://doi.org/10.1139/p60-150

Hofmann-Wellenhof, B., Lichtenegger, H., & Wasle, E. (2007). *GNSS–global navigation satellite systems: GPS, GLONASS, Galileo, and more*. Springer Science and Business Media.

Inchin, P., Snively, J., Kaneko, Y., Zettergren, M., & Komjathy, A. (2021). Inferring the evolution of a large earthquake from its acoustic impacts on the ionosphere. *AGU Advances*, *2*(2), e2020AV000260. https://doi.org/10.1029/2020AV000260

Inchin, P., Snively, J., Williamson, A., Melgar, D., Aguilar Guerrero, J., & Zettergren, M. (2020a). Mesopause airglow disturbances driven by nonlinear infrasonic acoustic waves generated by large earthquakes. *Journal of Geophysical Research: Space Physics*, *125*(6), e2019JA027628. https://doi.org/10.1029/2019JA027628

Inchin, P., Snively, J., Zettergren, M., Komjathy, A., Verkhoglyadova, O., & Tulasi Ram, S. (2020b). Modeling of ionospheric responses to atmospheric acoustic and gravity waves driven by the 2015 Nepal 7.8 Gorkha earthquake. *Journal of Geophysical Research: Space Physics*, *125*(4), e2019JA027200. https://doi.org/10.1029/2019JA027200

Inchin, P. A., & Snively, J. B. (2024). Supplemental materials to the manuscript "Three-dimensional numerical modeling of coseismic atmospheric dynamics and ionospheric responses in slant total electron content observations" [Dataset]. https://doi.org/10.17632/gn8rb3z846.1

Jia, Z., Jin, Z., Marchandon, M., Ulrich, T., Gabriel, A.-A., Fan, W., et al. (2023). The complex dynamics of the 2023 Kahramanmaraş, Turkey, Mw 7.8-7.7 earthquake doublet. *Science*, *381*(6661), 985–990. https://doi.org/10.1126/science.adi0685

Kaiser, A., Balfour, N., Fry, B., Holden, C., Litchfield, N., Gerstenberger, M., et al. (2017). The 2016 Kaikōura, New Zealand, earthquake: Preliminary seismological report. *Seismological Research Letters*, *88*(3), 727–739. https://doi.org/10.1785/0220170018

Kaneko, Y., & Goto, H. (2022). The origin of large, long-period near-fault ground velocities during surface-breaking strike-slip earthquakes. *Geophysical Research Letters*, *49*(10), e2022GL098029. https://doi.org/10.1029/2022gl098029

Komatitsch, D., & Tromp, J. (2002). Spectral-element simulations of global seismic wave propagation—Ii. Three-dimensional models, oceans, rotation and self-gravitation. *Geophysical Journal International*, *150*(1), 303–318. https://doi.org/10.1046/j.1365-246X.2002.01716.x

Komatitsch, D., & Vilotte, J.-P. (1998). The spectral element method: An efficient tool to simulate the seismic response of 2D and 3D geological structures. *Bulletin of the Seismological Society of America*, *88*(2), 368–392. https://doi.org/10.1785/bssa0880020368

Komjathy, A. (1997). *Global ionospheric total electron content mapping using the global positioning system*. Ph.D. dissertation (p. 248). Department of Geodesy and Geomatics Engineering Technical Report No. 188, University of New Brunswick.

Komjathy, A., Yang, Y.-M., Meng, X., Verkhoglyadova, O., Mannucci, A. J., & Langley, R. B. (2016). Review and perspectives: Understanding natural-hazards-generated ionospheric perturbations using GPS measurements and coupled modeling. *Radio Science*, *51*(7), 951–961. https://doi.org/10.1002/2015RS005910

Lee, R. F., Rolland, L. M., & Mikesell, D. T. (2018). Seismo-ionospheric observations, modeling, and back projection of the 2016 Kaikōura earthquake. *Bulletin of the Seismological Society of America*, *108*(3B), 1794–1806. https://doi.org/10.1785/0120170299

Maletckii, B., & Astafyeva, E. (2021). Determining spatio-temporal characteristics of coseismic travelling ionospheric disturbances (CTID) in near real-time. *Scientific Reports*, *11*(1), 20783. https://doi.org/10.1038/s41598-021-99906-5

Mannucci, A. J., Wilson, B. D., Yuan, D. N., Ho, C. H., Lindqwister, U. J., & Runge, T. F. (1998). A global mapping technique for GPS-derived ionospheric total electron content measurements. *Radio Science*, *33*(3), 565–582. https://doi.org/10.1029/97RS02707

Manta, F., Occhipinti, G., Feng, L., & Hill, E. M. (2020). Rapid identification of Tsunamigenic earthquakes using GNSS ionospheric sounding. *Scientific Reports*, *10*(1), 1–10. https://doi.org/10.1038/s41598-020-68097-w

Manta, F., Occhipinti, G., Hill, E. M., Perttu, A., Assink, J., & Taisne, B. (2021). Correlation between GNSS-tec and eruption magnitude supports the use of ionospheric sensing to complement volcanic hazard assessment. *Journal of Geophysical Research: Solid Earth*, *126*(2), e2020JB020726. https://doi.org/10.1029/2020jb020726

Martire, L., Krishnamoorthy, S., Vergados, P., Romans, L. J., Szilágyi, B., Meng, X., et al. (2023). The GUARDIAN system-a GNSS upper atmospheric real-time disaster information and alert network. *GPS Solutions*, *27*(1), 1–13. https://doi.org/10.1007/s10291-022-01365-6

McDonald, S. E., Drob, D. P., Emmert, J., Englert, C., Siskind, D., Huba, J., et al. (2012). The importance of thermospheric winds for ionospheric modeling. *A White Paper for the Decadal Survey of Solar and Space Physics*.

Nozuka, Y., Inchin, P. A., Kaneko, Y., Sabatini, R., & Snively, J. B. (2024). Earthquake source impacts on the generation and propagation of seismic infrasound to the upper atmosphere. *Geophysical Journal International*, *238*(1), 537–556. https://doi.org/10.1093/gji/ggae170

Occhipinti, G., Rolland, L., Lognonné, P., & Watada, S. (2013). From Sumatra 2004 to Tohoku-Oki 2011: The systematic GPS detection of the ionospheric signature induced by tsunamigenic earthquakes. *Journal of Geophysical Research: Space Physics*, *118*(6), 3626–3636. https://doi.org/10.1002/jgra.50322

Pelties, C., Gabriel, A., & Ampuero, J. (2013). Verification of an Ader-dg method for complex dynamic rupture problems. *Geoscientific Model Development Discussions*, *6*, 5981–6034.

Picone, J., Hedin, A. E., Drob, D. P., & Aikin, A. C. (2002). NRLMSISE-00 empirical model of the atmosphere: Statistical comparisons and scientific issues. *Journal of Geophysical Research*, *107*(A12), SIA15-1–SIA15-16. https://doi.org/10.1029/2002JA009430

Ravanelli, M., Occhipinti, G., Savastano, G., Komjathy, A., Shume, E. B., & Crespi, M. (2021). GNSS total variometeric approach: First demonstration of a tool for real-time tsunami genesis estimation. *Scientific Reports*, *11*(1), 3114. https://doi.org/10.1038/s41598-021-82532-6

Ren, X., Chen, J., Li, X., Zhang, X., & Freeshah, M. (2019). Performance evaluation of real-time global ionospheric maps provided by different IGS analysis centers. *GPS Solutions*, *23*(4), 1–17. https://doi.org/10.1007/s10291-019-0904-5

Rolland, L. M., Vergnolle, M., Nocquet, J.-M., Sladen, A., Dessa, J.-X., Tavakoli, F., et al. (2013). Discriminating the tectonic and non-tectonic contributions in the ionospheric signature of the 2011, mw7.1, dip-slip van earthquake, eastern Turkey. *Geophysical Research Letters*, *40*(11), 2518–2522. https://doi.org/10.1002/grl.50544

Roma-Dollase, D., Hernández-Pajares, M., Krankowski, A., Kotulak, K., Ghoddousi-Fard, R., Yuan, Y., et al. (2018). Consistency of seven different GNSS global ionospheric mapping techniques during one solar cycle. *Journal of Geodesy*, *92*(6), 691–706. https://doi.org/10.1007/s00190-017-1088-9

Sanchez, S. A., Kherani, E. A., Astafyeva, E., & de Paula, E. R. (2023). Rapid detection of co-seismic ionospheric disturbances associated with the 2015 IL lapel, the 2014 Iquique and the 2011 Sanriku-Oki earthquakes. *Journal of Geophysical Research: Space Physics*, *128*(9), e2022JA031231. https://doi.org/10.1029/2022JA031231

Savastano, G., Komjathy, A., Verkhoglyadova, O., Mazzoni, A., Crespi, M., Wei, Y., & Mannucci, A. J. (2017). Real-time detection of tsunami ionospheric disturbances with a stand-alone GNSS receiver: A preliminary feasibility demonstration. *Nature*, *7*(1), 46607. https://doi.org/10.1038/srep46607

Schliwa, N., & Gabriel, A.-A. (2024). Equivalent near-field corner frequency analysis of 3d dynamic rupture simulations reveals dynamic source effects. *Seismological Research Letters*, *95*(2A), 900–924. https://doi.org/10.1785/0220230225

Tanaka, T., Ichinose, T., Okuzawa, T., Shibata, T., Sato, Y., Nagasawa, C., & Ogawa, T. (1984). Hf-Doppler observations of acoustic waves excited by the Urakawa-Oki earthquake on 21 March 1982. *Journal of Atmospheric and Terrestrial Physics*, *46*(3), 233–245. https://doi.org/10.1016/0021-9169(84)90150-8

Taufiqurrahman, T., Gabriel, A.-A., Li, D., Ulrich, T., Li, B., Carena, S., et al. (2023). Dynamics, interactions and delays of the 2019 Ridgecrest rupture sequence. *Nature*, *618*(7964), 308–315. https://doi.org/10.1038/s41586-023-05985-x

Thomas, D., Bagiya, M. S., Sunil, P. S., Rolland, L., Sunil, A. S., Mikesell, T. D., et al. (2018). Revelation of early detection of co-seismic ionospheric perturbations in GPS-TEC from realistic modelling approach: Case study. *Scientific Reports*, *8*(1), 2045–2322. https://doi.org/10.1038/s41598-018-30476-9

Ulrich, T., Gabriel, A.-A., Ampuero, J.-P., & Xu, W. (2019). Dynamic viability of the 2016 Mw 7.8 Kaikōura earthquake cascade on weak crustal faults. *Nature Communications*, *10*(1), 1213. https://doi.org/10.1038/s41467-019-09125-w

Uphoff, C., Rettenberger, S., Bader, M., Madden, E. H., Ulrich, T., Wollherr, S., & Gabriel, A.-A. (2017). Extreme scale multi-physics simulations of the Tsunamigenic 2004 Sumatra megathrust earthquake. *Association for Computing Machinery*. https://doi.org/10.1145/3126908.3126948

Wielgosz, P., Milanowska, B., Krypiak-Gregorczyk, A., & Jarmołowski, W. (2021). Validation of GNSS-derived global ionosphere maps for different solar activity levels: Case studies for years 2014 and 2018. *GPS Solutions*, *25*(3), 103. https://doi.org/10.1007/s10291-021-01142-x

Zedek, F., Rolland, L. M., Mikesell, T. D., Sladen, A., Delouis, B., Twardzik, C., & Coïsson, P. (2021). Locating surface deformation induced by earthquakes using GPS, GLONASS and Galileo ionospheric sounding from a single station. *Advances in Space Research*, *68*(8), 3403–3416. https://doi.org/10.1016/j.asr.2021.06.011

Zettergren, M., & Hirsch, M. (2024). Gemini3D [Software]. *Zenodo*. https://doi.org/10.5281/zenodo.10475267

Zettergren, M., & Snively, J. (2015). Ionospheric response to infrasonic-acoustic waves generated by natural hazard events. *Journal of Geophysical Research*, *120*(9), 8002–8024. https://doi.org/10.1002/2015JA021116

Zettergren, M., & Snively, J. (2019). Latitude and longitude dependence of ionospheric tec and magnetic perturbations from infrasonic-acoustic waves generated by strong seismic events. *Geophysical Research Letters*, *46*(3), 1132–1140. https://doi.org/10.1029/2018GL081569